Using Multiple Images and Contours for Deformable 3D-2D Registration of a Preoperative CT in Laparoscopic Liver Surgery

Yamid Espinel[1], Lilian Calvet[1,2], Karim Botros[1], Emmanuel Buc[12], Christophe Tilmant[1], and Adrien Bartoli[1,2]

[1] EnCoV, Institut Pascal, UMR 6602 CNRS/UCA, Clermont-Ferrand, France
{yamid.espinel,karim.botros,christophe.tilmant,adrien.bartoli}@uca.fr
[2] University Hospital of Clermont-Ferrand, France
lilian.calvet@gmail.com
ebuc@chu-clermontferrand.fr

Abstract.

Purpose. Laparoscopic liver resection is a challenging procedure because of the difficulty to localise inner structures such as tumours and vessels. Augmented reality overcomes this problem by overlaying preoperative 3D models on the laparoscopic views. It requires deformable registration of the preoperative 3D models to the laparoscopic views, which is a challenging task due to the liver flexibility and partial visibility.

Methods. We propose several multi-view registration methods exploiting information from multiple views simultaneously in order to improve registration accuracy. They are designed to work on two scenarios: on rigidly related views and on non-rigidly related views. These methods exploit the liver's anatomical landmarks and texture information available in all the views to constrain registration.

Results. We evaluated the registration accuracy of our methods quantitatively on synthetic and phantom data, and qualitatively on patient data. We measured 3D target registration errors (TRE) in mm for the whole liver for the quantitative case, and 2D reprojection errors in pixels for the qualitative case.

Conclusion. The proposed rigidly related multi-view methods improve registration accuracy compared to the baseline single-view method. They comply with the 1 cm oncologic resection margin advised for hepatocellular carcinoma interventions, depending on the available registration constraints. The non-rigidly related multi-view method does not provide a noticeable improvement. This means that using multiple views with the rigidity assumption achieves the best overall registration error.

Keywords: Laparoscopy · Liver · Registration · Augmented Reality.

1 Introduction

Laparoscopy of liver is a surgical procedure that is becoming increasingly popular thanks to the reduced trauma and faster patient recovery times compared

to open surgery. However, the reduced intra-abdominal space and the lack of hand palpation make it difficult for surgeons to localise inner structures such as tumours and vessels. Surgeons often use laparoscopic ultrasound to find these structures; this is a complex technique, whose artefacts commonly impairs visibility and precise localisation. This can be a source of inaccurate tumour resections and undesired damage to the organ. Augmented Reality (AR) helps to solve this problem by overlaying a preoperative 3D model onto the intraoperative laparoscopic views. In this way, surgeons can see the real locations of the inner structures at any time, and guide the resection accordingly. The preoperative 3D model is reconstructed from CT or MRI data prior to the surgery, and is usually composed of the liver's parenchyma, tumours and vessels. From the moment such a 3D model is generated (preoperative stage) until the surgery day (intraoperative stage), the liver can deform significantly. Thus, a 3D-2D deformable registration is required to correctly align the preoperative 3D model to the views. This is a difficult problem in monocular laparoscopy, owing to the liver's strong deformations and partial visibility in the views.

Existing approaches make use of the liver's texture and anatomical landmarks to constrain registration. They can be classified as monocular [1–3] and non-monocular approaches [4–7, 9, 11, 12, 15], and their usage depends on the available equipment in the surgery room. We focus on the monocular case as it forms the standard in many surgical rooms. Among the existing monocular methods, some of them perform registration on a single view using anatomical landmarks [1, 2], while others use multiple views simultaneously using landmarks and keypoint correspondences [3]. A common issue with single-view approaches is the partial visibility of the liver in the image, owing to its large size and the reduced field of view of the endoscope. This reduces landmark visibility and negatively impacts registration accuracy. Regarding the multi-view approaches, they usually reconstruct an intraoperative 3D shape and use it as a target for registration. This reconstruction is usually done through SfM or SLAM. However, getting a reliable intra-operative shape is difficult and requires very good imaging conditions. Consequently, there is a need for monocular registration methods that are compatible with the clinical constraints and the desired clinical outcomes, such as improved positive resection margins and reduced adverse effects to the patient [16].

We propose several deformable registration methods that use multiple views simultaneously from standard monocular endoscopic systems. They bring the preoperative 3D models of the liver and its internal structures to camera coordinates, with the right shape deformation state. After registration is done, the 3D models of the inner structures are projected on and composed with the laparoscopic views. Our methods may assume that the liver does not deform between the laparoscopic views, which is the *rigidly related view case*, or that it may deform, which is the *non-rigidly related view case*, as illustrated by figure 1. We assume the views show the liver from multiple viewpoints. Our methods are based in [1], a method we refer to as Single-View (SV) in this article. SV combines visual cues with a biomechanical model to register the preoperative

3D model to a laparoscopic view. The visual cues consist of three different landmarks, namely the ridge, falciform ligament, and silhouette contours, as shown in Figure 1. The biomechanical properties are modeled using position-based dynamics with a Neo-Hookean elastic model [18]. For the rigidly related view case we propose 3 methods. The first one, named MV-B (for Multi-View Base), uses the liver landmarks and the inter-image rigidity as constraints for registration. The second one, named MV-B* (for Multi-View Base Improved), uses the same constraints as MV-B but, instead of computing the camera poses through ICP, it does so with Structure-from-Motion (SfM). The third one, named MV-C (for Multi-View Correspondences), uses available texture information via inter-image keypoint correspondences to constrain registration. These 3 methods produce a single deformed shape as output. For the non-rigidly related view case, we propose 1 method. It differs from the rigidly related ones in that it doesn't use the inter-image rigidity to solve registration. This method is named MV-D (for Multi-View Deformable) and uses the landmarks and keypoint correspondences as constraints, producing several deformed shapes according to the number of views. We illustrate and classify our methods, along with the constraints they use in figure 2.

We evaluated our methods quantitatively on phantom data and qualitatively on patient data. For the quantitative evaluation, target registration errors (TRE) were measured on uniformly-distributed control points inside the liver models. For the qualitative evaluation, the 2D reprojection errors of the registered livers were measured on control views. Our goal is to have a TRE of less than 1 cm, which is the safety resection margin advised for resection of Hepato-Cellular Carcinoma (HCC) [19]. We do not measure TRE on patient data due to the difficulty of having a reliable groundtruth with the available devices in the surgery room. We found that our multi-view methods are able to improve registration accuracy compared to the single-view case, being a step forward in AR for monocular laparoscopy of liver.
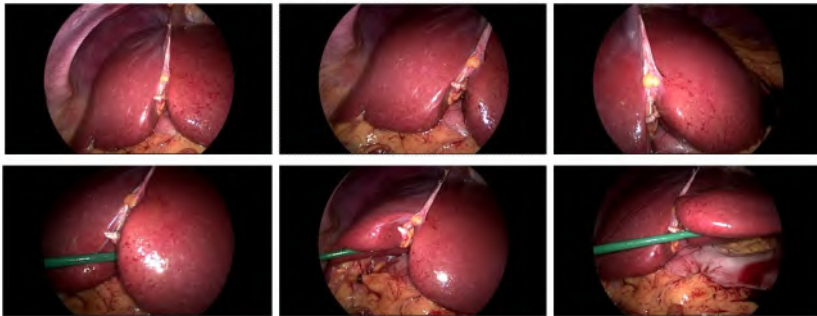
Fig. 1: Rigidly related (top) and non-rigidly related (bottom) laparoscopic views of the liver. The liver does not undergo noticeable deformations between the rigidly related views and may do between the non-rigidly related views.
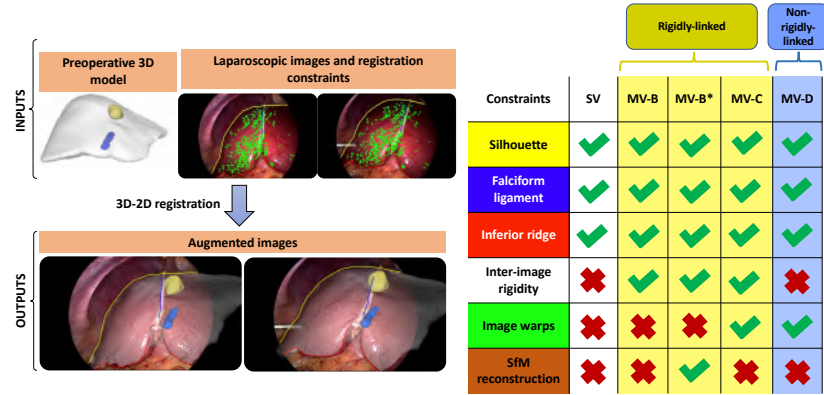
Fig. 2: Characteristics of the state-of-the-art and proposed registration methods.

2 Previous work

2.1 Monocular methods

The existing monocular approaches can use one or multiple views simultaneously to solve registration. They can be used with every monocular endoscopic system, being the standard in most surgery rooms. They use the available visual information to register the preoperative 3D models into the views in a rigid or a deformable fashion. Among the single-view methods, the one proposed in [2] uses the liver's silhouette contours along with a biomechanical model to perform 3D-2D deformable registration. Even if this method is able to fit the liver shape in the image, the use of generic silhouette landmarks gives the possibility of having multiple solutions for a single set of contours, and makes the method more sensible to initial rigid alignments. In an attempt to solve this issue, the method in [1] uses several types of landmarks that, combined together, are able to converge to an unique solution despite the initial alignment. Due to the partial visibility of the liver in the views, such single-view methods can only perform registration partially, leaving large regions of the preoperative 3D model unconstrained. Multiple-view methods try to solve this issue by combining the visual information coming from several views simultaneously, reconstructing an intraoperative shape through Structure-from-Motion (SfM) or SLAM. An example of multi-view registration with SfM is presented in [3], where the reconstructed intraoperative liver shape is used as a target for deformable registration. However, obtaining a reliable dense reconstruction requires very good imaging conditions that are not commonly available in laparoscopic liver surgery. Another example is found in [4], where a SLAM-based approach is used to reconstruct an

intraoperative shape and perform AR with it, with the possibility of making measurements and annotations on top of it. However, SLAM also requires good imaging conditions and a rigid scene to work properly.

2.2   Non-monocular methods

The non-monocular approaches are mainly used with stereoscopic endoscopes, sometimes including external tracking devices. A first example of intraoperative reconstruction using stereoscopic methods is found in [8], where a real-time stereo-matching algorithm is used to recover the liver intraoperative shape for registration purposes. However, no registration experiments are performed in this case. Another example is found in [7], where a rigid registration is made between the preoperative 3D models and a stereoscopically reconstructed set of patches. In order to localise the patches in 3D, an extra optical tracking system is required. A rigid registration method is also presented in [6], in which the preoperative models are aligned to the reconstructed intraoperative shape by minimizing the distance between multiple sets of 3D correspondences. They include automatically detected 3D features and manually annotated ridge contours in both shapes. A method that performs deformable registration is shown in [5], where an intraoperative shape obtained from stereoscopic techniques is used as a registration target. This method also uses the liver's boundaries and a biomechanical model as constraints for registration. A similar approach is presented in [9], where the preoperative 3D model is registered to an intraoperative shape using different types of landmarks, like the umbilical notch, the liver's anterior margin, and the vena cava. A deformable registration approach using deep learning is proposed in [10], where a CNN is trained and used to predict the deformation required to match a preoperative 3D model with an intraoperative shape. However, this method is highly sensible to initial rigid alignments.

3   Background

SV is a method that performs deformable registration of a preoperative 3D model M_0 into a single laparoscopic view I. It uses a Position Based Dynamics (PBD) approach with an isotropic Neo-Hookean elastic model [18] to obtain a deformed model M such that it approximates a set of constraints $\{C_B, C_C\}$, where C_B is the set of biomechanical constraints and Cc is the set of contour constraints [1]. The algorithm works in a Gauss-Seidel fashion, where each set of constraints $\{C_B, C_C\}$ is solved in an alternate way. The Neo-Hookean model works well for large deformations while being computationally inexpensive, and has also been validated for hepatic tissue [13, 14]. SV uses three types of contour landmarks: the ridge contour, located at the bottom of the liver's anterior side; the falciform ligament contour; and the silhouette contour corresponding to the occluding boundaries of the liver. They are illustrated in figure 2. These contours are marked on both the laparoscopic view and the preoperative 3D model prior to registration.

The algorithm of alternating biomechanical and contour projections used by SV is shown in Appendix 1 of the supplementary material. It takes as inputs the preoperative 3D model $\{M_0\}$ and the set of 2D and 3D contours C_C. Then, a main loop progressively deforms M by solving the biomechanical and contour constraints separately. The function **SolveBiomechanicalConstraints** follows the PBD approach from [18] to deform M in such a way that it complies with the volumetric constraints given by C_B. The function **SolveContourConstraints** projects the 3D contour vertices stored in C_C to their 2D counterparts and deforms M using PBD while keeping the projected vertices fixed. The loop iterates until the difference between the models of two consecutive iterations becomes lower than a threshold ϵ, or until a maximum number of iterations has passed.

4   Methodology

The main goal of our methods is to solve registration by using multiple laparoscopic views simultaneously. There should be a noticeable change of movement between the views, while keeping some overlap. This can be done by tilting and panning the laparoscope. Views from different trocars can also be used as long as there is overlapping between them. Using multiple views helps to overcome the partial visibility issue that is common in liver laparoscopy, improving the precision of registration compared to single-view methods. These methods perform registration for the rigidly related and non-rigidly related view cases. The former case involves making an additional assumption compared to the latter case, which is thus more general. Both cases are common; the former occurs primarily during the exploratory phase of surgery and the latter when the liver is mobilised during surgery. In the rigidly related case, MV-B, MV-B* and MV-C use the liver's rigidity to constrain registration. They all produce a single deformed shape, along with the corresponding camera poses for each of the views. In order to have suitable views for this case, the surgeon can pause the artificial ventilation system for a short period of time (about 10 seconds), while the scene is filmed. On top of the rigidity constraint, MV-B* and MV-C also use the inter-image keypoint correspondences as constraints for registration. MV-B* uses these correspondences to reconstruct an intraoperative pointcloud through Structure-from-Motion (SfM), while MV-C computes inter-image warp functions. Thus, the SfM reconstruction and the warp functions are used to constrain registration. For the non rigidly related view case, MV-D also computes inter-image warp functions from the keypoint correspondences, but does not use the rigidity constraint.

4.1   Multi-View Rigid Base (MV-B)

MV-B extends SV to solve registration on N rigidly related laparoscopic views. At each iteration, an SV refinement is done on every view and then, an average model is computed from all the views. To obtain this average model, all

the individual models from views $N > 1$ are transformed into the first view using transformation matrices computed through Absolute Orientation (ABSOR). Then, the average model is transformed back into all the views and a rigid ICP refinement is done in every view. The rigidity constraint comes thus from the averaging step, which produces a single deformed model.

The MV-B algorithm is shown in Appendix 2. The main function **MVBRegistration** takes as inputs the preoperative 3D model M_0 and the sets of 2D and 3D contours $\mathcal{C}_C = \{C_{C1}, ..., C_{CN}\}$ for every view I. A main loop performs SV registration on every view using the **SVRegistration** algorithm, computes the average model M from all the views using the **ComputeAverageModel** function, and rigidly registers M in every view using ICP through the **RigidICPRegistration** function. **ComputeAverageModel** first transforms all the models $\{M_{v2}, ..., M_{vN}\}$ into the first view using ABSOR and then proceeds to compute the average model M. The main loop iterates until the difference between the models of two consecutive iterations becomes lower than a threshold ϵ, or until a maximum number of iterations `max_iter` has passed. We have set $\epsilon = 10^{-3}$ and `max_iter` $= 100$ after running our methods for a large number of iterations on multiple phantom and patient cases.

4.2 Variant of Multi-View Rigid Base (MV-B*)

MV-B* is a variant of MV-B that, instead of computing inter-image rigid transformations using ABSOR, which may be inaccurate, directly uses the camera poses recovered by Structure-from-Motion (SfM). As such, SfM is firstly run on the keypoint correspondences extracted from SIFT, from which we obtain an intraoperative pointcloud P along with the camera poses. However, these SfM reconstructions are up to a scale factor s, which should be recovered in a precise way during the registration process. Obtaining a precise s can be a difficult task especially if we want to keep the process fully automatic. To achieve this, we rely on anisometry to find a metric that can indicate when a registration is done using the right s. Anisometry is a measure of shape variation that reflects to which extent a shape has stretched or shrunk locally, by integrating the local measures to form a global statistic. An anisometry measure vanishes if and only if the pair of shapes it is measured on are identical. Therefore, it is sensitive to scale changes, reaching its minimum value at the right scale. There are several ways of measuring anisometry on a discrete mesh model. The simplest way is to measure the Euclidean or geodesic distance between pairs of points chosen as the mesh vertices. We use three types of vertices to measure anisometry: the vertices defining the ridge landmark, the vertices forming the liver surface, and the vertices within the liver inner volume. We search for a suitable metric using both types of Euclidean and geodesic distances on the liver ridge, the liver surface and the liver inner volume, as shown in Appendix 3. The near anisometry measures are computed from connected pairs of vertex points and the far anisometry measures are computed from non-connected pairs of vertex points. The vertex pairs are selected randomly and the mean and median anisometry from all pairs are then used. Concretely, we have compared a total of 24 anisometry measures

on the phantom data (Euclidean vs geodesic, ridge vs surface vs volume, near vs far, mean vs median). To measure anisometry, we first look for an interval around a correct s for which MV-B* has a better registration accuracy than SV. Then, we run MV-B* by varying s around the previously defined interval and measure the aforementioned anisometry measures between the preoperative and the registered models. We did these experiments on $M = 2$ different phantoms, using $L = 10$ combinations of views per phantom. Finally, we compute a global mean anisometry A from all the phantoms and all the view combinations, as:

$$A = \frac{\sum_{i=1}^{M} \delta_m}{M}. \tag{1}$$

We use δ_m, the mean of the anisometry measures for phantom m, computed as:

$$\delta = \frac{\sum_{l=1}^{L} \alpha_l}{L}. \tag{2}$$

We use α_l as either the mean or median of the anisometry measures for view combination l, computed as:

$$\alpha_{\text{mean}} = \frac{\sum_{p=1}^{P} |D_{F_p} - D_{I_p}|}{P} \tag{3}$$

$$\alpha_{\text{median}} = \text{med}_{p \in [1,P]}(|D_{F_p} - D_{I_p}|), \tag{4}$$

where P is the number of vertex pairs and $\{D_{I_p}, D_{F_p}\}$ are the initial preoperative and final registered distances for the point pair p. These distances can be either Euclidean or geodesic.

After running MV-B* on the 2 phantoms by varying s within $\pm 12\%$ around the ground-truth, we found that the Euclidean near volume anisometry shows the desired convex behavior with its minimum value at the ground-truth. The behavior of all the 24 anisometry measures is shown in Appendix 4. Using this metric, we run MV-B* starting from an initial s and look for the minimum anisometry through a bisection search strategy. In the end, the resulting deformed model M is the product of a registration using the right s.

The algorithm for MV-B* is shown in Appendix 5. The main function **MV-B*Registration** uses bisection search to search for a local minimum in anisometry and perform registration with the correct scale s. It starts by doing single-view registration using the **SVRegistration** function to obtain an initial middle scale s_M. This scale is computed as the depth ratio of the closest points between the registered 3D model M and the SfM pointcloud P. From the initial s_M, a lower and upper pair of interval bounds $\{s_L, s_U\}$ is set as $\pm 30\%$ of s_M. Then, multi-view registration is done on $\{s_L, s_U\}$ by scaling the SfM camera poses $\mathcal{T}$ and calling the **DeformableRegistration** function. The respective anisometries D_L, D_U are then computed. A main loop then compares D_L against D_U and selects the sub-interval s_L, s_M or s_M, s_U that has the lowest anisometry. The new middle scale s_M is thus computed, multi-view registration is run on s_M and the new interval bound D_L or D_U will correspond to the anisometry of

s_M depending on the chosen sub-interval. The loop iterates until the difference between the lower and upper bounds becomes lower than ϵ and deems the scale to be found. The resulting model M is thus the one obtained using the last middle scale s_M.

4.3   Multi-View Rigid with Correspondences (MV-C)

MV-C is an extension of MV-B that uses the inter-image keypoint correspondences to constrain registration. This strengthens the contour correspondences with the more reliable keypoint correspondences in the ICP refinement stage. The keypoint correspondences are obtained using SIFT and the mismatches are filtered out using FBDSD [20]. They are used to compute inter-image warp transformation functions η_{ji}, which are based on the Rigid-Perspective Thin-Plate Spline [17]. The image warp η_{ji} allow one to transfer any point from view j to view i. It is used to iteratively minimise the Euclidean distance between the projected particles, transferred to a common reference view i. This allows one to estimate an average, optimal camera pose, by ensuring that the P model particles x_p, $p \in [1, P]$, are projected to the same location of the liver surface in all the views. First, each visible model particle x_p in the reference view i is projected in every view j wherever it is visible. Second, these 2D particle projections are transferred from all views j into the reference view i using η_{ji}. Third, a barycenter point b is computed in view i as the average of the transferred points. Fourth, b is used as the 2D correspondence of the model point x_p to refine camera pose. Fifth, the four steps are repeated, choosing each view as the reference view in turn, so as to refine its camera pose. In the end, MV-C generates a single deformed model M from the contour, the inter-image correspondence and the rigidity constraints given by all the views.

The MV-C algorithm is shown in Appendix 6. As a first step, the keypoint correspondences K_C are extracted from the views using SIFT and the warp functions η are computed. Then, a main loop progressively deforms M in 4 stages: First, SV registration is done on every view using the **SVRegistration** algorithm. Second, the average model M is computed from all the views using the **ComputeAverageModel** function. Third, the inter-image projection distances of the model particles x_p are minimised by transferring the 2D projections of the particles from view m to n using the warp function η_{mn}, and then by computing a set barycentric points b_n from the transferred particles x_{pmn} using the **BarycentersFromTransferredParticles** function. Fourth, the barycentric points b_n and the 2D-3D contours C_C are used to rigidly register M in every view through the **RigidICPRegistration** function. The loop iterates until the difference between the models of two consecutive iterations becomes lower than a threshold $\epsilon = 10^{-3}$, or until a maximum number of iterations `max_iter` $= 100$ has passed.

4.4   Multi-View Deformable with Correspondences (MV-D)

MV-D is a variant of MV-C that does not use the inter-image rigidity to solve registration, but keeps the inter-image correspondences and the contours $\mathcal{C}_C$ as constraints for registration. Compared to MV-C, MV-D produces multiple shapes M_N according to the number of views used and the liver deformations in each of them. This is particularly useful in cases where the liver is being manipulated by tools or other external forces.

   The algorithm for MV-D is shown in Appendix 7. The procedure is similar to MV-C with the difference that no average model is computed from all the views. Instead, the individually deformed models $\{M_{v1}, ..., M_{vN}\}$ are rigidly register with ICP in every view using the correspondences between the 2D projections of the visible particles and their corresponding barycenters b, along with the set of contour landmarks $\mathcal{C}_C$. Barycenters b are also obtained after transferring the particles from other views using the warp functions η.

5   Experimental results

5.1   Rigidly related views

Phantom data. We reconstructed a 3D liver mesh from a patient's CT and generated 10 virtual deformations using Abaqus [21], by simulating gravity, pneumoperitoneum and manipulations with surgical instruments. We added randomly-spaced carved markers in the model's surface to simulate keypoints. We 3D printed these deformations using PLA (Polylactic Acid). Then, we used a surgical laparoscope and a pelvitrainer box to take 10 views of every printed model. Laparoscopic views of the 10 phantoms are shown in Appendix 8. We implemented our methods using Qt and unoptimized C++ code, and they were run on a PC with a processor AMD Ryzen 7 3700x, a graphics card NVIDIA RTX 2080 Ti, 32 GB of RAM, and with Ubuntu 20.04. We estimated registration for every phantom by varying the number of views, going from 1 to 8, and measured TRE as the average prediction error for uniformly sampled points within the virtual 3D liver. The contour marking is done manually in less than 5 minutes for all the 8 views. We use 8 views as a maximum to keep the computation time reasonable. The results are shown in figure 3(a). We observe that the TRE for SV is steady around (11.89 ± 7.77) mm, that for MV-B it varies with the number of views from (10.21 ± 5.87) mm to (12.08 ± 12.46) mm, that for MV-B* it remains steady around (10.77 ± 6.26) mm, that for MV-C it consistently decreases until (8.32 ± 4.58) mm, and that for MV-D it has a maximum at (14.14 ± 7.24) mm for 2 views and a final value of (12.58 ± 6.69) mm. MV-B* estimated SfM scales close to the groundtruth, with differences comprised between -13% and +7%. In order to better observe the performance of MV-B* using a sufficiently good scale, we computed TRE for phantoms with lower than 5% scale variation. This corresponds to 7 out of 10 phantoms, with performance shown in figure 3(b). In this case, MV-B* has better performance than SV, with a TRE of (9.86 ± 6.36) mm vs (10.91 ± 6.41) mm. The total running time using

8 views, after marking the contours, was of 2'48" for MV-B, 5'37" for MV-B*, 4'52" for MV-C, and 4'28" for MV-D.

Patient data. We collected CT and laparoscopic data from 5 patients. We reconstructed the preoperative 3D models from the CT data and selected 9 random representative laparoscopic views for each patient. Out of these views, one was singled out to serve as control view. The control view is not used to perform registration but rather to verify registration, measuring the landmark prediction error expressed in pixels, using the registration computed on other views and rigidly adapted to the control view. Examples of these rigidly related patient views are shown in Appendix 9. We measure the reprojection errors due to the difficulty of having a reliable groundtruth to compute TRE in 3D. We only run MV-B, MV-C and MV-D for the 8 views. MV-B* failed to obtain a reliable SfM reconstruction. The results are is shown in figure 4(a). We observe a clear benefit of using multiple views for registration, especially for the rigidly related methods.

5.2   Non-rigidly related views

Phantom data. We ran all methods on the generated phantom data, on 10 combinations of 8 views, with every view corresponding to a different deformation. MV-B* was excluded, as SfM could not be ran in the absence of rigidity. TRE results for a varying number of views are shown in figure 3(c). For the experiments using 8 views, SV has a TRE of (11.59 ± 6.95) mm on the control points, MV-B has a TRE of (13.34 ± 9.51) mm, MV-C has a TRE of (11.03 ± 9.45) mm, and MV-D has a TRE of (10.71 ± 6.35) mm.

Patient data. We selected 9 random representative views per patient from the previously described data with significant liver deformation across the views. As for the rigidly related view case, we singled out one view to serve as control view. Examples of such non-rigidly related patient views are shown in Appendix 10. Landmark prediction error is computed on the control views and expressed in pixels. The results are shown in figure 4(b). We ran MV-B, MV-C and MV-D for the 8 views. We observed a 1 mm improvement when using multiple views to solve registration.

6   Conclusions

The proposed multi-view methods improve registration accuracy compared to the single-view method, especially for rigidly related views. The MV-C method is the best performing one in this case, with an improvement of 2.45 mm over SV on the phantom data. In comparison, MV-D is the worst performing method in the rigidly related case. These results were confirmed on the patient data, where MV-C improves the reprojection error by 15 px over SV. Its performance also

(a)

(b)

(c)
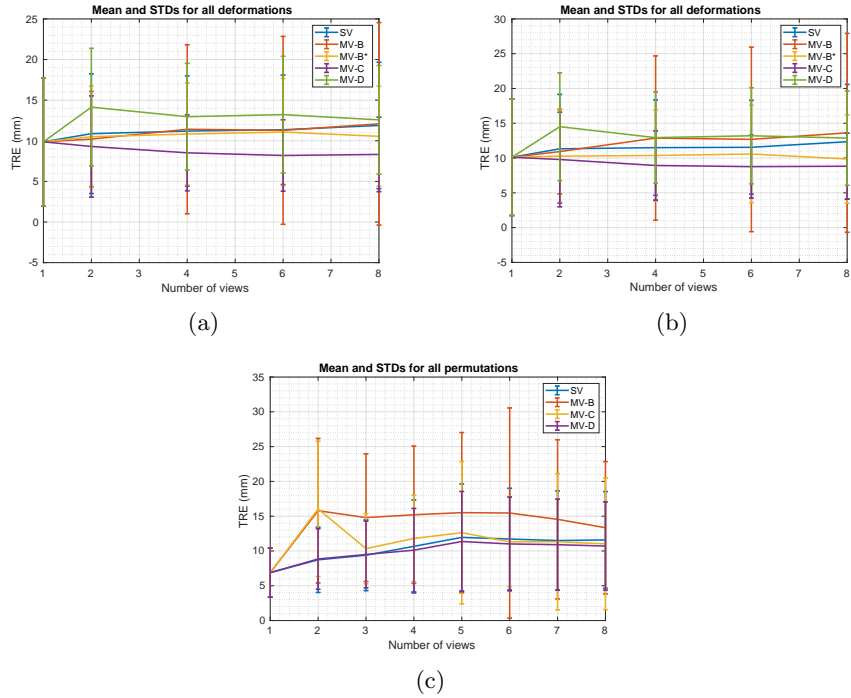
Fig. 3: Mean TRE and standard deviations using all the methods on the rigidly related views from all the 10 phantoms (a) and on phantoms with estimated scale with less than 5% of deviation (b), and using all the methods on the non-rigidly related views from all the phantoms (c).

Patient	SV	MV-B	MV-C	MV-D
1	26.07	21.98	**19.49**	28.61
2	58.40	10.28	**09.49**	42.73
3	42.78	32.24	**29.75**	44.15
4	**17.13**	21.72	21.13	23.79
5	26.71	**15.46**	16.95	24.28
average	34.28	20.33	**19.36**	32.71

(a)

Patient	SV	MV-B	MV-C	MV-D
1	32.47	36.82	30.49	**30.14**
2	63.08	69.37	66.48	**57.62**
3	**46.24**	54.41	49.91	49.79
4	25.07	36.44	29.79	**21.31**
5	31.85	36.82	32.15	**29.75**
average	39.74	46.77	41.76	**37.73**

(b)

Fig. 4: Control view errors (px) on patient data for (a) rigidly related methods with best results in bold and second best underlined and (b) non-rigidly related methods with best results in bold.

varies with the number of views, although it becomes steady beyond 6 views. The MV-B* method also works better than SV if a sufficiently good scale is found. However, it is difficult to obtain a reliable SfM reconstruction on patient data, which limits the usage of this method. When using non-rigidly related views, MV-D behaves similarly to SV and MV-C, with a slight improvement of 1 mm.

Visual inspection on the error distribution shows that TRE follows a unimodal distribution with positive skewness. As future work, we plan to work on *(i)* improving registration accuracy in the non-rigidly related view case, *(ii)* reducing the registration time by automatically detecting the anatomical landmarks, and *(iii)* using additional information to improve in both the rigidly and non-rigidly related view cases, such as probing liver points with the tip of the surgical tools. As part of the second goal, we are currently running the Preoperative to Intraoperative Laparoscopic Fusion challenge (P2ILF) [22] in MICCAI 2022, with the objective of automatically detecting the landmark correspondences between the laparoscopic views and the preoperative 3D models.

7   Compliance with ethical standards

Yamid Espinel declares to have no potential conflicts of interest. Lilian Calvet declares to have no potential conflicts of interest. Karim Botros declares to have no potential conflicts of interest. Emmanuel Buc declares to have no potential conflicts of interest. Christophe Tilmant declares to have no potential conflicts of interest. Adrien Bartoli declares to have no potential conflicts of interest.

All procedures involving human participants were in accordance with the ethical standards of the institutional and/or national research committee and with the 1964 Helsinki declaration and its later amendments or comparable ethical standards. This study is also supported by an ethical approval with ID IRB00008526-2019-CE58 issued by CPP Sud-Est VI in Clermont-Ferrand, France.

Informed consent was obtained from the patients included in the study.

References

1. Koo, B., Ozgur, E., Le Roy, B., Buc, E., Bartoli, A.: Deformable registration of a preoperative 3D liver volume to a laparoscopy image using contour and shading cues. MICCAI, (2017)
2. Adagolodjo, Y., Trivisonne, R., Haouchine, N., Cotin, S., Courtecuisse, H.: Silhouette-based pose estimation for deformable organs application to surgical augmented reality. IROS, (2017)
3. Modrzejewski, R., Collins, T., Seeliger, B., Bartoli, A., Hostettler, A., Marescaux, J.: An in vivo porcine dataset and evaluation methodology to measure soft-body laparoscopic liver registration accuracy with an extended algorithm that handles collisions. IPCAI, (2019)
4. Chen, L., Tang, W., John, N.W., Wuan, T.R., Zhang, J.J.: SLAM-based dense surface reconstruction in monocular minimally invasive surgery and its application to augmented reality. Computer Methods and Programs in Biomedicine, 158, 135-146 (2018)
5. Haouchine, N., Roy, F., Untereiner, L., Cotin, S.: Using contours as boundary conditions for elastic registration during minimally invasive hepatic surgery. IROS, (2016)

6. Robu, M.R., Ramalhinho, J., Thompson, S., Gurusamy, K., Davidson, B., Hawkes, D., Stoyanov, D., Clarkson, M.: Global rigid registration of CT to video in laparoscopic liver surgery. International Journal of Computer Assisted Radiology and Surgery, 13, 947–956 (2018)

7. Thompson, S., Totz, J., Song, Y., Johnsen, S., Stoyanov, D., Ourselin, S., Gurusamy, K., Schneider, C., Davidson, B., Hawkes, D., Clarkson, M.: Accuracy validation of an image guided laparoscopy system for liver resection. Proceedings of SPIE - The International Society for Optical Engineering 9415(09):1-12, (2015)

8. Totz, J., Thompson, S., Stoyanov, D., Gurusamy, K., Davidson, B., Hawkes, D., Clarkson, M.: Fast semi-dense surface reconstruction from stereoscopic video in laparoscopic surgery. IPCAI, (2014)

9. Plantefeve, R., Peterlik, I., Haouchine, N., Cotin, S.: Patient-specific biomechanical modeling for guidance during minimally-invasive hepatic surgery. Annals of Biomedical Engineering, 44, 139-153, (2016)

10. Pfeiffer, M., Riediger, C., Leger, S., Kühn, J., Seppelt, D., Hoffmann, R., Weitz, J., Speidel, S. Non-Rigid Volume to Surface Registration using a Data-Driven Biomechanical Model. MICCAI, (2020)

11. Clements, L., Collins, J., Weis, J., Simpson, A., Kingham, T., Jarnagin, W. Miga, M.: Deformation correction for image guided liver surgery: An intraoperative fidelity assessment. Surgery, 162(3): 537-547, (2017)

12. Bernhardt, S., Nicolau, S., Bartoli, A., Agnus, V., Soler, L., Doignon, C.: Using Shading to Register an Intraoperative CT Scan to a Laparoscopic Image. Computer-Assisted and Robotic Endoscopy. CARE, (2015)

13. Chui, C., Kobayashi, E., Chen, X., Hisada, T., Sakuma, I., Combined compression and elongation experiments and non-linear modelling of liver tissue for surgical simulation. Medical and Biological Engineering and Computing, 44, 787–798, (2004)

14. Shi, H., Farag, A., Fahmi, R., Chen, D.: Validation of Finite Element Models of Liver Tissue Using Micro-CT. IEEE transactions on bio-medical engineering, 55, 978-984, (2008)

15. Plantefeve, R., Peterlik, I., Haouchine, N., Cotin, S.: Patient-specific Biomechanical Modeling for Guidance During Minimally-invasive Hepatic Surgery. Annals of Biomedical Engineering, 44, 139-153, (2016)

16. Thompson, S., Hu, M., Johnsen, S., Gurusamy, K., Davidson, B., Hawkes, D.: Towards Image Guided Laparoscopic Liver Surgery, Defining the System Requirement. LIVIM, (2011)

17. Bartoli, A., Perriollat, M., Chambon, S.: Generalized Thin-Plate Spline Warps. International Journal of Computer Vision, 88, 85-110, (2010)

18. Bender, J., Koschier, D., Charrier, P., Weber, D.: Position-based Simulation of Continuous Materials. Computer & Graphics, (2014)

19. Zhong, FP., Zhang, YJ., Liu, Y., Zou, SB. Prognostic impact of surgical margin in patients with hepatocellular carcinoma: A meta-analysis. Medicine, 96(37):e8043, (2017)

20. Pizarro, D., Bartoli, A. Feature-Based Deformable Surface Detection with Self-Occlusion Reasoning. International Journal of Computer Vision, 97, 54-70, (2010)

21. 3DS Abaqus, http://edu.3ds.com/en/software/abaqus-student-edition. Last accessed 2 Mar 2021

22. Ali, S., Espinel, Y., Jin, Y., Maier-Hein, L., A. Bartoli. (2022, March 18). Preoperative to Intraoperative Laparoscopy Fusion (P2ILF). MICCAI, (2022). https://p2ilf.grand-challenge.org/